

A spatially localized architecture for fast and modular DNA computing

Gourab Chatterjee¹, Neil Dalchau², Richard A. Muscat³, Andrew Phillips^{2*} and Georg Seelig^{3,4*}

Cells use spatial constraints to control and accelerate the flow of information in enzyme cascades and signalling networks. Synthetic silicon-based circuitry similarly relies on spatial constraints to process information. Here, we show that spatial organization can be a similarly powerful design principle for overcoming limitations of speed and modularity in engineered molecular circuits. We create logic gates and signal transmission lines by spatially arranging reactive DNA hairpins on a DNA origami. Signal propagation is demonstrated across transmission lines of different lengths and orientations and logic gates are modularly combined into circuits that establish the universality of our approach. Because reactions preferentially occur between neighbours, identical DNA hairpins can be reused across circuits. Co-localization of circuit elements decreases computation time from hours to minutes compared to circuits with diffusible components. Detailed computational models enable predictive circuit design. We anticipate our approach will motivate using spatial constraints for future molecular control circuit designs.

Human-engineered systems, from ancient irrigation networks to modern semiconductor circuitry, rely on spatial constraints to guide the flux of materials and information. Cells similarly use spatial organization¹ through enzyme scaffolds^{2,3} or organelles⁴ to perform complex information-processing tasks within a crowded intracellular environment^{5,6}. Such spatial constraints play a pivotal role, by accelerating interactions between components that are closer together and reducing interference between those that are further apart. Not surprisingly, spatial organization has been recognized as a potentially powerful engineering principle for the construction of synthetic molecular circuitry. However, in practice, synthetic circuits have so far relied almost exclusively on interactions between diffusible components guided by chemical specificity^{7–9}. As a result, scaling up such circuits for complex and parallel computation rapidly becomes intractable due to the limited availability of orthogonal components. Here, we demonstrate a novel design paradigm for realizing scalable molecular logic circuits with a minimal set of orthogonal components, using spatial organization rather than sequence specificity as the main organizing principle. DNA nanotechnology provides an ideal framework for exploring the use of spatial constraints in molecular circuit design. First, DNA origami forms a uniquely programmable scaffold for the controlled arrangement of molecular circuit elements¹⁰. Second, research on DNA-based walking motors corroborates the notion that programmed, multi-step reactions can occur in DNA systems with spatial constraints. Over the last decade, such DNA walking motors, mainly powered by enzyme catalysis, have progressed from being able to make a small number of externally triggered steps to autonomously moving along multi-step tracks laid out on a DNA origami^{11–14}. Walking motors could, in principle, be programmed to perform computation^{15–17}. However, by considering that only information needs to propagate in a computational circuit, rather than a specific motor molecule, we open up a much broader design space for engineering. Third, DNA strand displacement^{18,19} provides a mechanism for the rational design and implementation of complex digital^{20,21} and analog²² circuits,

neural networks²³ and reaction diffusion patterns²⁴, with quantitatively predictable behaviours. Such DNA strand displacement circuits form a benchmark for success, but also pose a set of challenges that need to be overcome through novel design approaches. In particular, circuit operation is slow at experimentally realistic concentrations. Furthermore, unintentional binding interactions between sequences degrade performance and increase with circuit size, leading to a lack of modularity in circuit design and execution.

Several theoretical papers have proposed DNA circuit architectures that take advantage of spatial constraints to overcome these limitations of speed and modularity^{25–28}. Limiting interactions to spatially proximal circuit elements should result in faster reactions, because spatial localization allows the effective concentrations of components to be increased substantially compared to components in solution. Moreover, sequences can be reused across components because proximity rather than chemical specificity controls information flow. Recent experimental work has begun to characterize the kinetics of strand displacement reactions with localized components, providing evidence for an increase in circuit speed due to localization^{29–31}, and elementary localized DNA logic gates have also been built^{32,33}. However, an experimental realization of a scalable circuit architecture that exploits the advantages of spatial organization is still lacking.

Here, we experimentally demonstrate a modular design strategy—the ‘DNA domino’ architecture—that uses spatial organization to realize fast arbitrary logic at the molecular scale. Domino gates and signal transmission lines (wires) are realized with DNA hairpins laid out on a DNA origami scaffold (Fig. 1a and Supplementary Fig. 1). In practice, hairpins were localized on the origami scaffold by extending the appropriate origami staple strands with the hairpin sequences. After assembly, origamis were purified to remove unincorporated hairpins. The reaction mechanism underlying circuit operation reimagines the hybridization chain reaction (HCR)³⁴, such that polymerization occurs along designed trajectories on a DNA substrate²⁵. All reactions are rationally designed and, unlike

¹Department of Bioengineering, University of Washington, Seattle, Washington 98195, USA. ²Microsoft Research, Cambridge CB1 2FB, UK. ³Department of Electrical Engineering, University of Washington, Seattle, Washington 98195, USA. ⁴Paul G. Allen School of Computer Science & Engineering, University of Washington, Seattle, Washington 98195, USA. *e-mail: gseelig@uw.edu; andrew.phillips@microsoft.com

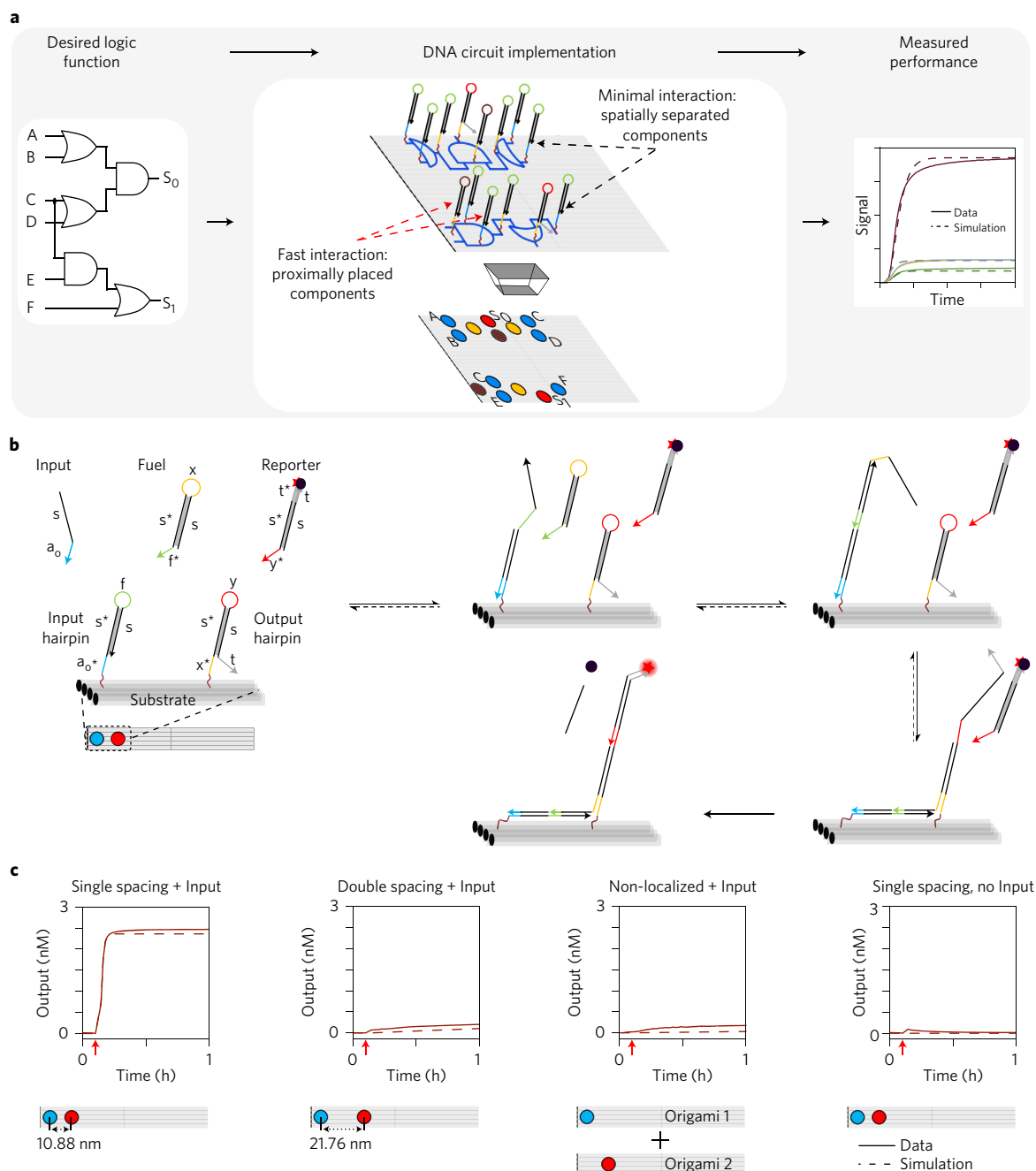


Figure 1 | Spatial organization controls signal propagation. **a**, High-level abstraction of the circuit design process. An abstract logic circuit (left) is realized using DNA hairpin components arranged on a DNA origami (middle), tested experimentally and compared with model simulation (right). A top view of the localized circuit on origami (middle, bottom) shows the four basic hairpins reused for all circuits in this Article as colour-coded circles (Input hairpin (HP): blue; Intermediate hairpin: yellow; Output hairpin: red; Threshold hairpin: brown). **b**, Reaction mechanism for a two-hairpin domino (2HP) wire. Arrows denote 3' ends. Functional domains are indicated by colour and labelled in the first panel (s: stem domain; a_o , x, f, y, t: toehold domains; s^* : a domain complementary to s). **c**, Unquenched fluorophore concentration plots (solid lines) and corresponding simulations (dashed lines) demonstrating signal transfer across localized and non-localized versions of a 2HP wire. Left to right: single-spaced 2HP wire; double-spaced 2HP wire; Input hairpin and Output hairpin on different origami; single-spaced 2HP wire without Input. Reactions were carried out at 25 °C with 5 nM Origami, 40 nM Reporter, 100 nM Fuel, 50 nM Input in 1× TAE, 12.5 mM Mg^{2+} . Red arrows indicate time points when input strands were added.

most DNA walking motors, no enzyme or ribozyme catalysis is required for operation.

Localized signal propagation mechanism

To illustrate how information is propagated spatially, we consider the 'DNA domino effect' in a minimal two-hairpin wire composed of an Input and Output hairpin attached to a DNA origami scaffold (Fig. 1b). In each reaction step, a hairpin stem is unwound, and a

toehold that is initially sequestered in the hairpin loop becomes available to initiate the unwinding of a subsequent hairpin stem. The Input hairpin is opened by binding of an Input strand, which enables the capture of a diffusible Fuel hairpin. Requiring a diffusible Fuel ensures that no unwanted reactions can occur between Input and Output hairpins during initial assembly of the origami. Previous theoretical work proposed an alternative fully localized architecture that does not require a diffusible Fuel^{26,27}.

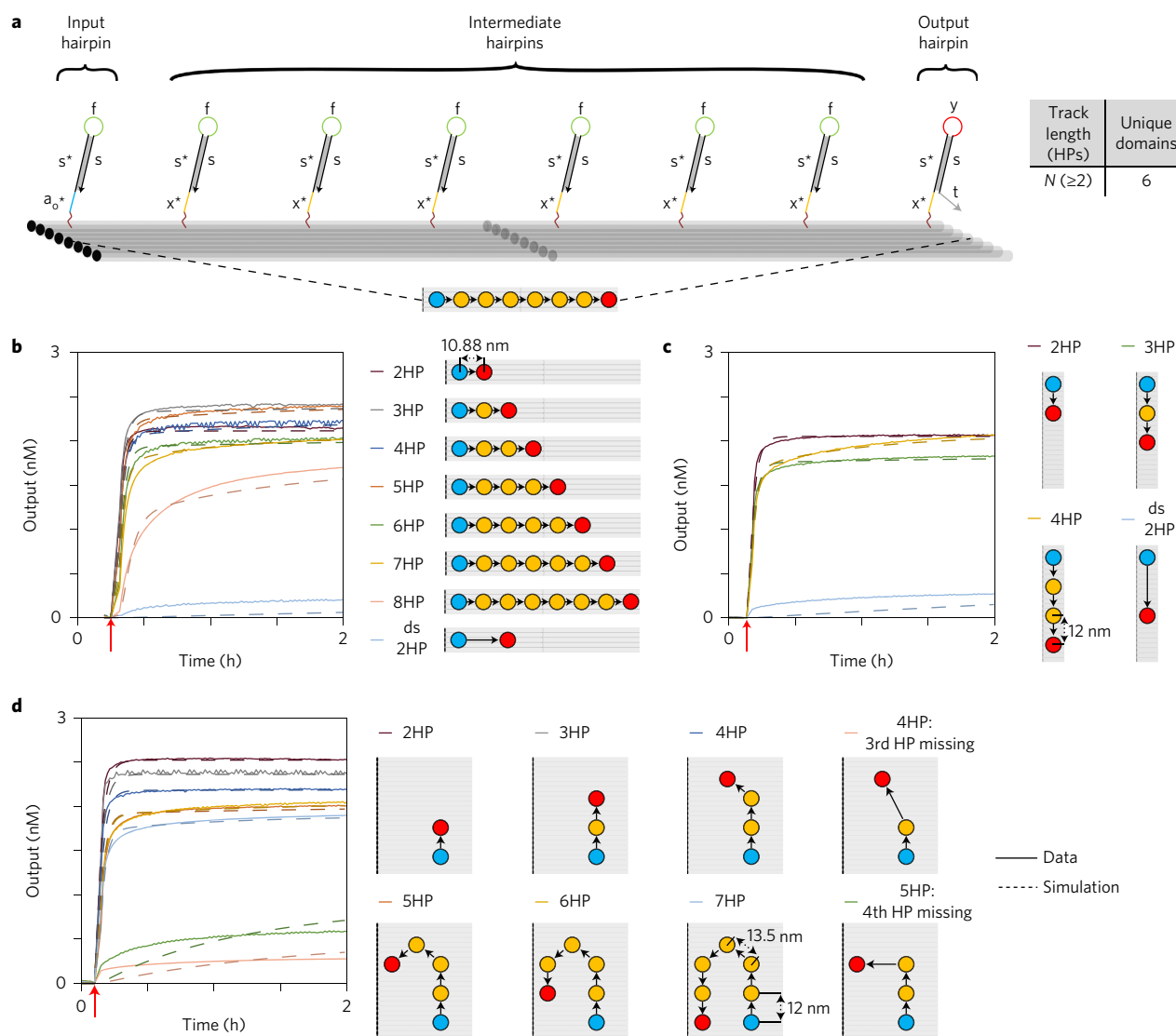


Figure 2 | Signals propagate along wires of different lengths and orientations. **a**, Schematic representation of an untriggered eight-hairpin (8HP) wire along the DNA origami helical axis (domains are labelled with lowercase letters). Bottom: top view of the wire with Input hairpin (blue circle), six identical Intermediate hairpins (yellow circles) and Output hairpin (red circle). Right: wires of arbitrary lengths can be built with only six unique domains. **b–d**, Signal propagation along the helical axis (**b**, 2–8 HP), perpendicular to the helical axis (**c**, 2–4 HP) and through a 180° turn (**d**, 2–7 HP). Left: unquenched fluorophore concentration plots (solid lines) and simulations (dashed lines). Reactions were carried out at 25 °C with 5 nM Origami, 40 nM Reporter, 200 nM Fuel, 50 nM Input in 1× TAE, 12.5 mM Mg^{2+} . Right: graphical depiction of all different wires. Hairpin spacing is consistent along the vertical (12 nm), horizontal (10.88 nm) and diagonal (13.5 nm) directions. Black arrows indicate the sequence of signal propagation. Red arrows indicate time points when inputs were added. 'ds 2HP' represents a double-spaced two-hairpin wire.

Although such a localized fuel architecture could enable faster computation, care also needs to be taken to avoid spurious leaks between fully localized components²⁷. In practice, the Fuel can be added in large excess over the concentrations of the other components and thus does not substantially limit the reaction speed. The Output hairpin is opened by the Fuel-bound Input hairpin via a fast local interaction. Finally, the activated Output hairpin displaces the quencher-labelled strand from the diffusible Reporter complex, resulting in increased Reporter fluorescence.

To demonstrate the benefits of spatial organization, we experimentally compared signal propagation between Input and Output hairpins, positioned at different distances from each other or on different scaffolds (Fig. 1c). We first confirmed that a signal could rapidly propagate across proximally positioned Input and Output hairpins (single spacing) in a two-hairpin wire ($t_{1/2} < 3$ mins). No detectable signal transfer was observed without Input addition.

We then doubled the distance between Input and Output hairpins (double spacing) on the same origami and showed that separating the hairpins beyond their theoretical maximum reach resulted in minimal signal transfer (Fig. 1c and Supplementary Fig. 6). Furthermore, we found that interactions between Input and Output hairpins on two different origamis were significantly slower than single-spaced hairpin interactions on the same origami and comparable to the double-spaced hairpin interactions. Crucially, decreasing the operating concentration of the origamis did not affect the speed of localized intra-origami signal propagation, but significantly reduced the speed of non-localized inter-origami interactions (Supplementary Fig. 7). Finally, we performed kinetics experiments with two-hairpin wires that had undergone 0, 1, 2 or 3 rounds of purification and found that leak reactions due to unincorporated staples were mostly eliminated after the third round (Supplementary Fig. 3).

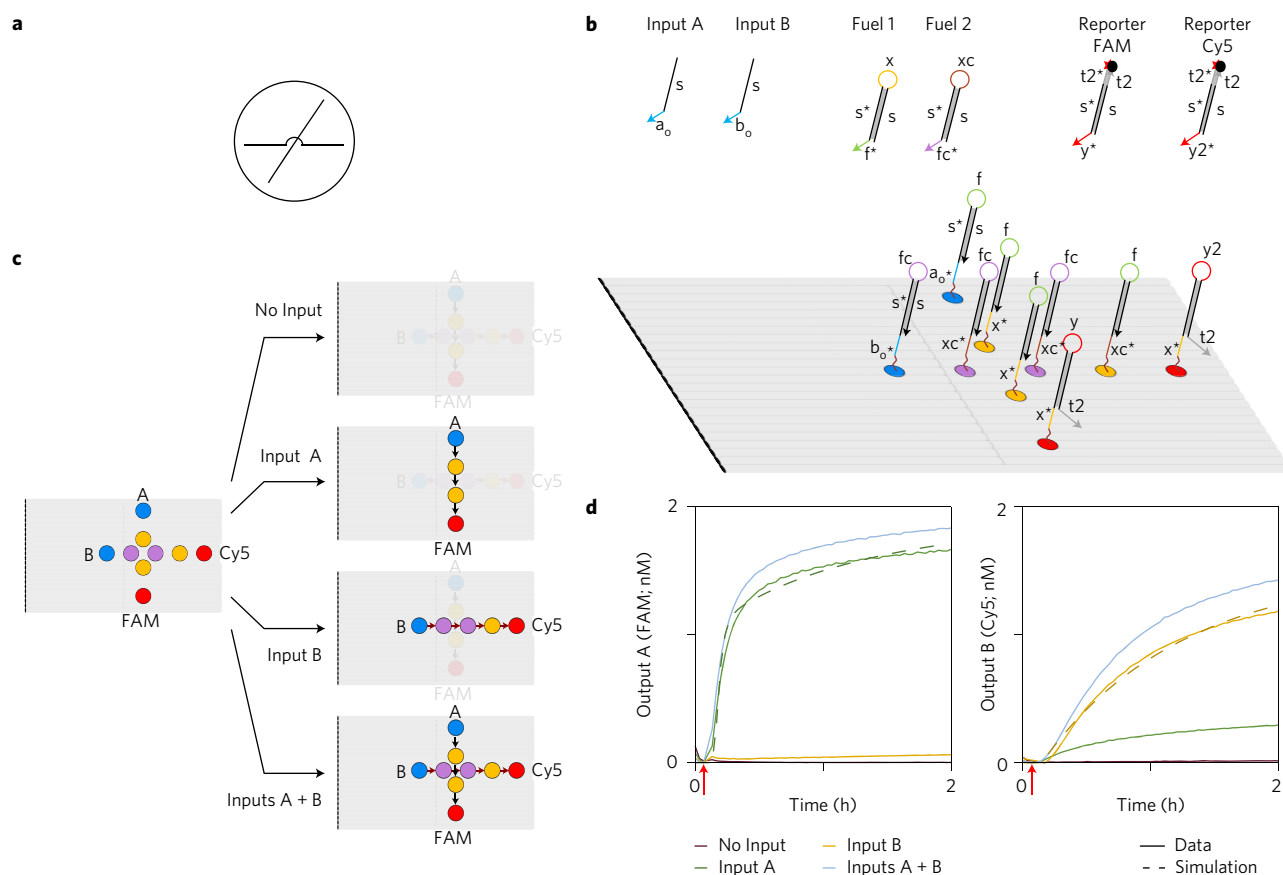


Figure 3 | Design and implementation of a wire crossover. **a**, Wire crossover diagram. **b**, Domain-level representation of a wire crossover. Functional domains are indicated by colour and labelled with lowercase letters. The two wires use orthogonal toeholds (x^* , xc^*) and hairpin loop domains (f , fc) at the junction. Matching fuel species are used for each orthogonal wire. **c**, Schematic representation of signal transmission for different Input combinations. Input A and Input B trigger wires that activate spectrally distinct reporters, FAM and Cy5, respectively. **d**, Signal transfer through wire crossover leading to downstream activation of Reporter FAM (left) and Reporter Cy5 (right). Colours of the graphs correspond to different cases of Input addition as described in the legend. Reactions were carried out at 25 °C with 5 nM Origami, 20 nM Reporter(s), 100 nM Fuel(s), 50 nM Input(s) in 1× TAE, 12.5 mM Mg^{2+} . Red arrows indicate when Inputs were added.

We quantified the kinetics of domino circuits by constructing detailed computational models and parameterizing them using experimental data (Supplementary Figs 9–22 and Supplementary Section 15). Interactions involving a diffusible molecule and a tethered hairpin were modelled as bimolecular reactions according to mass action kinetics, while interactions between two complexes tethered to the same origami were converted to unimolecular reactions by scaling with a local concentration^{27,35,36}. We used parameter inference techniques to establish a maximum likelihood parameter set (Supplementary Fig. 18). By ensuring that equivalent interactions in different circuits were parameterized with the same rate constants, we were able to demonstrate consistency in the quantitative behaviour of our circuits. In this way, models were used throughout this study for the design and optimization of circuit behaviour.

Signal propagation through molecular wires

We created wires of varying lengths and orientations (Supplementary Figs 1 and 25) to allow signal propagation over extended distances, by using Intermediate hairpins (Supplementary Fig. 26) as signal-relaying components. Multiple identical Intermediate hairpins were positioned at appropriate distances (single spacing) to relay the signal from an Input to an Output hairpin. A schematic of an untriggered eight-hairpin domino wire is shown in Fig. 2a. We experimentally observed fast and reliable signal propagation through wires with up to eight hairpins (spanning over 80 nm)

along the origami helical axis ($t_{1/2} < 10$ min, Fig. 2b), with up to four hairpins perpendicular to this axis ($t_{1/2} < 6$ min, Fig. 2c) and with up to seven hairpins through a 180° turn ($t_{1/2} < 10$ min, Fig. 2d). We observed significantly reduced signal propagation whenever an Intermediate hairpin was intentionally omitted and found that signals propagated preferentially via neighbouring hairpins (Supplementary Fig. 27). Signal completion levels varied approximately inversely with track length (Supplementary Figs 28 and 29), probably due to imperfect incorporation of hairpins into the origami (Supplementary Fig. 30). The non-monotonic decrease in signal can be explained by position-dependent hairpin incorporation efficiency (Supplementary Fig. 31). Signal production due to inter-origami interactions increased with the number of hairpins, but even for an eight-hairpin wire was considerably lower than signal production through localized interactions. As noted previously, lowering the origami concentrations significantly reduced inter-origami interactions, with minimal effect on the speed of localized signal propagation (Supplementary Figs 7, 8, 32 and 33).

A wire crossover module

Wires may need to cross at various positions to optimize the spatial layout of localized circuits. A wire crossover module (Fig. 3a) is implemented by using orthogonal toehold and hairpin loop sequences for the two different wires at the junction (Fig. 3b). Specifically, toehold and hairpin loop sequences in one of the crossing wires are temporarily ‘translated’ to avoid interference. The

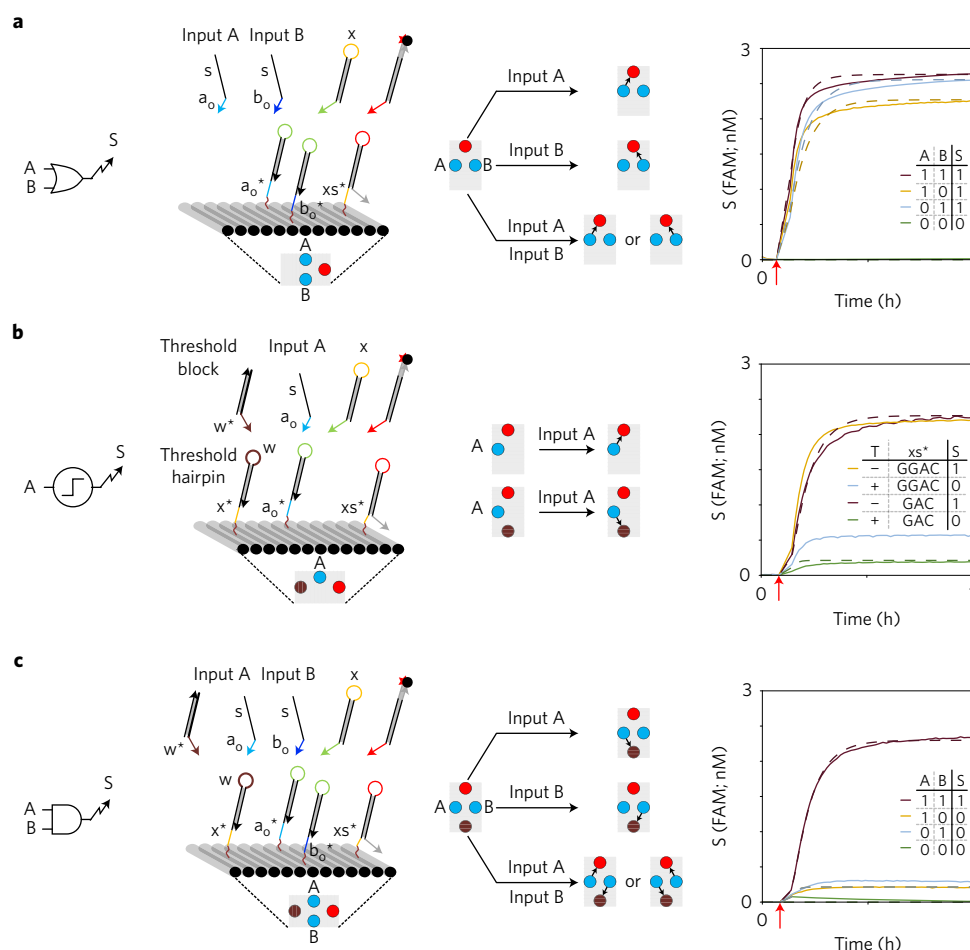


Figure 4 | Elementary logic gates are realized with localized DNA hairpins. **a**, Two-input OR. **b**, Thresholding module. **c**, Two-input AND. First column: logic gate diagram. Second column: DNA domino representation and top view projection. All domains are labelled with lowercase letters and Inputs are distinguished by their toeholds (a_o and b_o , blue). The output toehold domain x^* (yellow, 3 or 4 nt) is a truncated version of x^* (6 nt). Third column: graphical summary of circuit operation. For OR and AND gates, the response to different input combinations is depicted. For the threshold module, a circuit with a Threshold hairpin is compared to a circuit without it. Black arrows indicate the (most likely) direction of signal propagation. Fourth column: unquenched fluorophore concentration plots (solid lines) and simulations (dashed lines). For AND and OR gates, legends are represented as truth tables, where the presence of an input strand (A,B) or output signal (S) is denoted by '1' and their absence is denoted by '0'. For the Threshold module, the T column indicates whether the system did (+) or did not (–) include the Threshold hairpin, which contains the x^* domain (CTGGAC). The x^* column indicates whether the Output hairpin has a 3 nt (GAC) or 4 nt (GGAC) toehold. Experimental conditions were as in Fig. 1. Red arrows indicate when inputs were added.

translation is initiated by using a different hairpin loop sequence in the hairpin before the junction (Input hairpin of B track, Fig. 3b). The translated signal then proceeds across the junction before being reverted to its original form in the hairpin loop of the Intermediate hairpin following the junction (fourth hairpin of the B track, Fig. 3b). Because the orthogonal toehold and hairpin loop domains are used only at the crossover junctions, they can be reused in all crossovers in a localized circuit, promoting simplicity in circuit design. Experimentally, minimal output signal was observed through the participating wires in the absence of the corresponding Inputs, but upon addition of both Inputs, both signals successfully crossed over each other at the junction (Fig. 3c,d). We also found that the dynamics of each wire of the crossover circuit were consistent with our parameterized model (Fig. 3d and Supplementary Fig. 24).

Design and construction of elementary logic gates

As a prerequisite for performing arbitrary logic computation with our domino architecture, we next designed two-input OR and AND gates. The two-input OR domino gate was implemented

through a wire 'fan-in' by positioning an Output hairpin close to two orthogonal Input hairpins on the origami (Fig. 4a). Because all hairpin components were constrained to have the same stem, Input orthogonality was ensured by using distinct toehold sequences. Experimentally, no significant output fluorescence was observed in the absence of both Inputs, but the addition of either one or both Inputs resulted in high output fluorescence, consistent with OR logic ($t_{1/2} < 5$ min).

To implement a two-input AND domino gate, we used a thresholding strategy to prevent signal propagation when only one of the inputs is present. Specifically, a 'Threshold' hairpin was designed to block signal propagation by outcompeting the Output hairpin. We ensured preferential binding to the Threshold hairpin by shortening the Output hairpin toehold, while keeping the Threshold hairpin toehold at 6 nt (Fig. 4b and Supplementary Fig. 34). Once the Threshold hairpin is opened, it captures a partially double-stranded 'Threshold block', making signal inhibition practically irreversible. Experimentally, the extent of preferential binding to the Threshold hairpin depended on the difference in toehold lengths (Fig. 4b), where a 3 nt Output

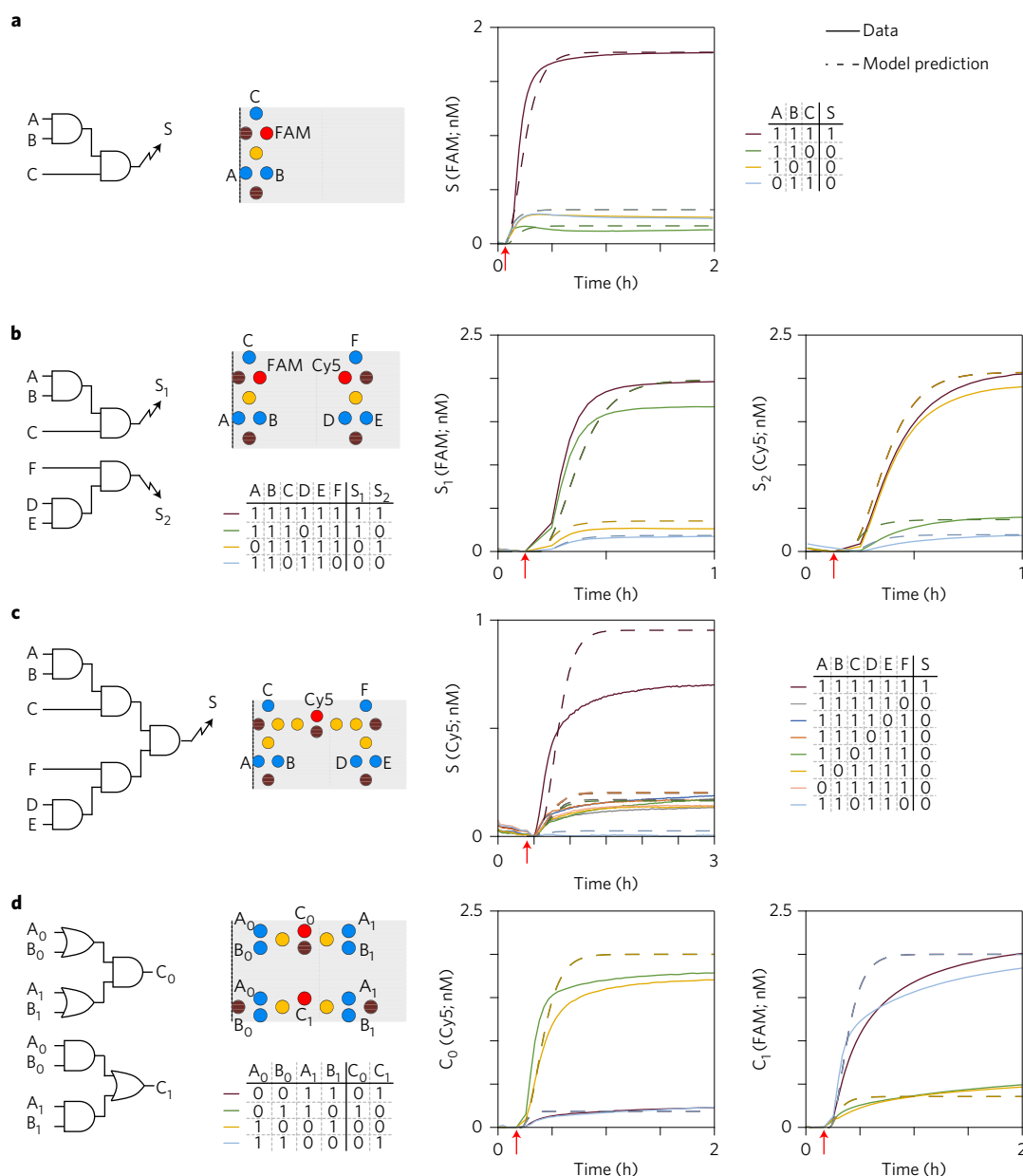


Figure 5 | Elementary logic gates are combined into multi-input logic circuits. a, Three-input AND gate. **b**, Two three-input AND gates in parallel. Spectrally distinct reporters are used to measure the output of the two gates simultaneously. **c**, Six-input AND gate. **d**, Two-input dual-rail XNOR gate. Left column: logic circuit diagram. Middle column: top view of the localized DNA circuit. Right column: unquenched fluorophore concentration plots (solid lines) and model predictions (dashed lines). Legends are represented as truth tables, where presence of an Input or Output is denoted by '1' and their absence is denoted by '0'. Reactions were carried out at 25 °C with 5 nM Origami, 40 nM Reporter(s), 200 nM Fuel, 50 nM Input(s) in 1× TAE, 12.5 mM Mg²⁺. Red arrows indicate when inputs were added.

hairpin toehold was found to be optimal. Consequently, all domino logic circuits presented in this study, including the OR gate discussed above, were constructed using Input and Threshold hairpins with 6 nt toeholds and Intermediate and Output hairpins with 3 nt toeholds.

The two-input AND domino gate was implemented by combining an OR gate with a Threshold hairpin. The Output and Threshold hairpins were positioned at equal distances to two orthogonal Input hairpins (Fig. 4c). When only one of the Input strands is added, the Threshold hairpin blocks signal propagation, resulting in low output fluorescence. When both Input strands are added, the signal from one of the Inputs is blocked, while the signal from the other Input successfully propagates to the Output

hairpin and generates high output fluorescence ($t_{1/2} < 6$ min), consistent with two-input AND logic.

The measurements of the two-input OR, threshold and two-input AND gates were included in the parametrization of our computational models. Kinetic parameters for Input and Fuel binding were shared between all circuits. However, we used distinct local concentration parameters for the wires and logic circuits, because the spacing between hairpins was slightly different in these two settings. The ratio between the binding rates of the Threshold and the Output hairpin was also calibrated to the experimental data and was ~10:1 (Supplementary Fig. 18). The simulated model behaviours were consistent with the measured kinetics for the two-input OR, threshold and two-input AND gates (Fig. 4 and Supplementary Fig. 19).

Modular cascading of logic gates for complex logic circuits

To demonstrate modular circuit design using our domino architecture, we built a three-input AND gate by cascading a pair of two-input AND gates on the same origami. Specifically, we replaced the Output hairpin of an upstream two-input AND gate with an Intermediate hairpin, such that the output of the first gate was relayed to the input of the second (Fig. 5a and Supplementary Fig. 35). Following the addition of any combination of two Input strands, the circuit showed low output fluorescence. When all three Input strands were added there was high output fluorescence ($t_{1/2} < 6$ min), consistent with three-input AND logic. Furthermore, the experimental data exhibited the expected Boolean logic. We were able to quantitatively predict the dynamics of the three-input AND gate through model simulation, using the parameters obtained from our previously characterized circuits (Fig. 5a).

Next, we positioned two distinct three-input AND gates side by side and triggered them simultaneously to determine whether multiple circuits on the same origami can function concurrently (Fig. 5b). Both gates used the same Intermediate and Threshold hairpins throughout, along with the universal Fuel, but used distinct toeholds for the Input and Output hairpins to ensure orthogonality. Experimental measurements were consistent with model predictions (Fig. 5b).

To further demonstrate scalability, we constructed a six-input AND gate by connecting the outputs of both three-input AND gates, using an additional two-input AND gate (Fig. 5c and Supplementary Fig. 36). When all six Inputs were added, the circuit produced high output signal ($t_{1/2} \sim 12$ min). Conversely, the circuit produced low output for any combination of five or fewer Inputs. Although the number of hairpins increased from four for the two-input AND gate to eighteen for the six-input AND gate, all hairpins used the same conserved set of only five domains, plus a separate domain for each input and output. Similar to our experiments on wires, we observed attenuation of the output signal with increasing number of hairpins (Supplementary Fig. 29). This signal loss can in part be explained with a model assuming a fixed non-zero probability of hairpin omission (Supplementary Fig. 30). Assuming a hairpin incorporation efficiency of 83% resulted in the best fit of our model for the logic circuits data, while a fit to the wire data suggests an efficiency of 93%. Our estimates are broadly consistent with a previous experimental study reporting an 87.5% average staple incorporation efficiency in a single-layer origami³⁷.

To exemplify arbitrary Boolean logic computation using our domino architecture, we built a two-input dual-rail XNOR gate (Fig. 5d and Supplementary Fig. 37). Dual-rail encoding allows an arbitrary Boolean logic function to be realized using only a combination of AND and OR gates, avoiding the need for NOT gates, which are difficult to implement experimentally²¹. Each input variable A is specified as TRUE by a dedicated signal strand A₁ and specified as FALSE by a distinct signal strand A₀ (Fig. 5d). Only one of the two strands is present at any given time. Accordingly, our dual rail XNOR gate was implemented as a pair of parallel circuits, computing TRUE and FALSE outputs separately. The complete circuit arranged 17 hairpins into six two-input AND and OR gates. The experimental data showed signal propagation ($t_{1/2} < 8$ min), consistent with predictions from the computational model.

Conclusions

Overall, the number of unique sequences required for building any complex domino circuit did not depend on the number of constituent gates, but only on the number of inputs and outputs. Moreover, if wire crossovers are required, the same crossover toehold and hairpin sequences can be reused for any number of crossover points. Our domino circuits also performed significantly faster

than previous systems with diffusible components (Supplementary Table 2). For example, a three-input AND domino gate had a $t_{1/2}$ of 7 min with an operating concentration of only 2 nM, compared to 4 h for an equivalent circuit with diffusible components operated at 100 nM concentration²¹.

The modularity of our design approach enabled us to construct a family of cascaded circuits spanning an entire rectangular tile origami. Even larger and more complex circuit designs could be made with bigger and multilayered stiffer origami scaffolds, but three issues would need to be addressed. First, inputs are currently distinguished only by their toehold domains and in practice the number of sufficiently orthogonal 6 nt toeholds is small. This limitation can be overcome by incorporating an additional recognition domain in the Input hairpin, to encode input specificity (Supplementary Fig. 38). Second, we observed signal attenuation with increasing circuit size, probably due to imperfect hairpin incorporation. Such imperfections will become less limiting with continuing improvements in origami assembly protocols. Alternatively, component redundancy could be used to compensate for assembly defects, and signal restoration modules (for example, a threshold coupled with an amplification step²¹) could be used to restore the signals at the ensemble level once the localized computation has completed. Third, although inter-origami interactions are not currently limiting, they could become significant as circuit size increases. Such interactions could be reduced by using a low concentration of logic-processing origami, followed by global signal amplification of the ensemble output. More generally, inter-origami interactions can be further reduced by using immobilizing techniques to tether origami molecules to a surface, or by using closed three-dimensional origamis with components tethered to the inner faces.

Circuit architectures with localized components may provide a path towards the delivery of DNA circuits to cells, a long-held ambition of dynamic DNA nanotechnology that only recently started to become reality^{38–40}. Not only do localized circuits enable control of stoichiometry during delivery, but increased speed compared to non-localized circuits may be even more pronounced in the densely packed cellular environment. Moreover, localized circuits could be used to increase the complexity of chemical synthesis reactions achievable with DNA-templated chemistry^{41,42} or to enhance the specificity of theranostic DNA robots⁴³.

Methods

Methods and any associated references are available in the [online version of the paper](#).

Received 19 December 2016; accepted 1 June 2017;
published online 24 July 2017

References

1. Agapakis, C., Boyle, P. & Silver, P. Natural strategies for the spatial optimization of metabolism in synthetic biology. *Nat. Chem. Biol.* **8**, 527–535 (2012).
2. Good, M., Zalatan, J. & Lim, W. Scaffold proteins: hubs for controlling the flow of cellular information. *Science* **332**, 680–686 (2011).
3. Morrison, D. & Davis, R. Regulation of MAP kinase signaling modules by scaffold proteins in mammals. *Annu. Rev. Cell Dev. Biol.* **19**, 91–118 (2003).
4. Sweetlove, L. J. & Fernie, A. R. The spatial organization of metabolism within the plant cell. *Annu. Rev. Plant Biol.* **64**, 723–746 (2013).
5. Ellis, R. J. Macromolecular crowding: an important but neglected aspect of the intracellular environment. *Curr. Opin. Struct. Biol.* **11**, 114–119 (2001).
6. Konopka, M. C., Shkel, I. A., Cayley, S. & Record, M. T. Crowding and confinement effects on protein diffusion *in vivo*. *J. Bacteriol.* **188**, 6115–6123 (2006).
7. Polka, J. K., Hays, S. G. & Silver, P. A. Building spatial synthetic biology with compartments, scaffolds, and communities. *Cold Spring Harb. Perspect. Biol.* **8**, a024018 (2016).
8. Park, S.-H., Zarrinpar, A. & Lim, W. Rewiring MAP kinase pathways using alternative scaffold assembly mechanisms. *Science* **299**, 1061–1064 (2003).
9. Delebecque, C., Lindner, A., Silver, P. & Aldaye, F. Organization of intracellular reactions with rationally designed RNA assemblies. *Science* **333**, 470–474 (2011).

10. Rothmund, P. W. Folding DNA to create nanoscale shapes and patterns. *Nature* **440**, 297–302 (2006).
11. Wickham, S. F. *et al.* A DNA-based molecular motor that can navigate a network of tracks. *Nat. Nanotech.* **7**, 169–173 (2012).
12. Muscat, R. A., Bath, J. & Turberfield, A. J. A programmable molecular robot. *Nano Lett.* **11**, 982–987 (2011).
13. Gu, H., Chao, J., Xiao, S.-J. & Seeman, N. A proximity-based programmable DNA nanoscale assembly line. *Nature* **465**, 202–205 (2010).
14. Lund, K. *et al.* Molecular robots guided by prescriptive landscapes. *Nature* **465**, 206–210 (2010).
15. Boemo, M. A., Lucas, A. E., Turberfield, A. J. & Cardelli, L. The formal language and design principles of autonomous DNA walker circuits. *ACS Synth. Biol.* **5**, 878–884 (2016).
16. Dannenberg, F., Kwiatkowska, M., Thachuk, C. & Turberfield, A. DNA walker circuits: computational potential, design, and verification. *Nat. Comput.* **14**, 195–211 (2015).
17. Mo, D., Lakin, M. & Stefanovic, D. Scalable design of logic circuits using an active molecular spider system. In *Proc. 10th International Conference on Information Processing in Cells and Tissues* (eds Lones, M., Tyrrell, A., Smith, S. & Fogel, G.) 13–28 (Lecture Notes in Computer Science 9303, Springer, 2015).
18. Yurke, B., Turberfield, A., Mills, A., Simmel, F. & Neumann, J. A DNA-fuelled molecular machine made of DNA. *Nature* **406**, 605–608 (2000).
19. Zhang, D. Y. & Seelig, G. Dynamic DNA nanotechnology using strand-displacement reactions. *Nat. Chem.* **3**, 103–113 (2011).
20. Seelig, G., Soloveichik, D., Zhang, D. Y. & Winfree, E. Enzyme-free nucleic acid logic circuits. *Science* **314**, 1585–1588 (2006).
21. Qian, L. & Winfree, E. Scaling up digital circuit computation with DNA strand displacement cascades. *Science* **332**, 1196–1201 (2011).
22. Chen, Y.-J. J. *et al.* Programmable chemical controllers made from DNA. *Nat. Nanotech.* **8**, 755–762 (2013).
23. Qian, L., Winfree, E. & Bruck, J. Neural network computation with DNA strand displacement cascades. *Nature* **475**, 368–372 (2011).
24. Chirieleison, S. M., Allen, P. B., Simpson, Z. B. & Ellington, A. D. Pattern transformation with DNA circuits. *Nat. Chem.* **5**, 1000–1005 (2013).
25. Muscat, R., Strauss, K., Ceze, L. & Seelig, G. DNA-based molecular architecture with spatially localized components. *ACM SIGARCH Comp. Architect. News - ICSA '13* **41**, 177–188 (2013).
26. Chandran, H., Gopalkrishnan, N., Phillips, A. & Reif, J. in *DNA Computing and Molecular Programming* Vol. 6937 (eds Cardelli, L. & Shih, W.) 64–83 (Springer, 2011).
27. Dalchau, N., Chandran, H., Gopalkrishnan, N., Phillips, A. & Reif, J. Probabilistic analysis of localized DNA hybridization circuits. *ACS Synth. Biol.* **4**, 898–913 (2015).
28. Qian, L. & Winfree, E. in *DNA Computing and Molecular Programming* (eds Murata, S. & Kobayashi, S.) 114–131 (Springer, 2014).
29. Teichmann, M., Kopperger, E. & Simmel, F. C. Robustness of localized DNA strand displacement cascades. *ACS Nano* **8**, 8487–8496 (2014).
30. Dunn, K. E., Trefzer, M. A., Johnson, S. & Tyrrell, A. M. Investigating the dynamics of surface-immobilized DNA nanomachines. *Sci. Rep.* **6**, 29581 (2016).
31. Ruiz, I. M. *et al.* Connecting localized DNA strand displacement reactions. *Nanoscale* **7**, 12970–12978 (2015).
32. Gerasimova, Y. & Kolpashchikov, D. Towards a DNA nanoprocessor: reusable tile-integrated DNA circuits. *Angew. Chem. Int. Ed.* **128**, 10400–10403 (2016).
33. Jung, J., Hyun, D. & Shin, Y. in *Proceedings of Computer Design (ICCD), 2015 33rd IEEE International Conference* 259–265 (IEEE, 2015).
34. Dirks, R. M. & Pierce, N. A. Triggered amplification by hybridization chain reaction. *Proc. Natl Acad. Sci. USA* **101**, 15275–15278 (2004).
35. Genot, A. J., Zhang, D. Y. & Bath, J. Remote toehold: a mechanism for flexible control of DNA hybridization kinetics. *J. Am. Chem. Soc.* **133**, 2177–2182 (2011).
36. Lakin, M. R., Petersen, R., Gray, K. E. & Phillips, A. in *DNA Computing and Molecular Programming* (eds Murata, S. & Kobayashi, S.) 132–147 (Springer, 2014).
37. Jungmann, R., Avendaño, M. S., Dai, M. & Woehrstein, J. B. Quantitative super-resolution imaging with qPAINT. *Nat. Methods* **13**, 439–442 (2016).
38. Chen, Y.-J. J., Groves, B., Muscat, R. A. & Seelig, G. DNA nanotechnology from the test tube to the cell. *Nat. Nanotech.* **10**, 748–760 (2015).
39. Groves, B., Chen, Y. J., Zurla, C. & Pochekailov, S. Computing in mammalian cells with nucleic acid strand exchange. *Nat. Nanotech.* **11**, 287–294 (2015).
40. Hemphill, J. & Deiters, A. DNA computation in mammalian cells: microRNA logic operations. *J. Am. Chem. Soc.* **135**, 10512–10518 (2013).
41. He, Y. & Liu, D. Autonomous multistep organic synthesis in a single isothermal solution mediated by a DNA walker. *Nat. Nanotech.* **5**, 778–782 (2010).
42. Meng, W. *et al.* An autonomous molecular assembler for programmable chemical synthesis. *Nat. Chem.* **8**, 542–548 (2016).
43. Douglas, S. M., Bachelet, I. & Church, G. M. A logic-gated nanorobot for targeted transport of molecular payloads. *Science* **335**, 831–834 (2012).

Acknowledgements

The authors thank K. Strauss and L. Ceze for their support in initiating this project and F. Randisi for assistance with oxDNA simulations. This work was supported by National Science Foundation grants CCF-1409831, CCF-1317653 and IIS-1212940 and Office of Naval Research grant N00014-13-1-0880 to G.S. G.C. was partially supported by Microsoft Research Ltd.

Author contributions

G.C., N.D., R.A.M., A.P. and G.S. designed the experiments and wrote the paper. G.C. performed the experiments. N.D. and A.P. performed the modelling studies.

Additional information

Supplementary information is available in the [online version of the paper](#). Reprints and permissions information is available online at www.nature.com/reprints. Publisher's note: Springer Nature remains neutral with regard to jurisdictional claims in published maps and institutional affiliations. Correspondence and requests for materials should be addressed to A.P. and G.S.

Competing financial interests

The authors declare no competing financial interests.

Methods

Component design. All the hairpins used in this study were designed with a 12 nt stem to provide metastability while preventing any unnecessary loss of speed and chemical potential due to branch migration through longer domains. The toehold domains were also chosen to be 6 nt long for optimal strand displacement speed. The domino wires were built with three basic components: Input hairpin, Intermediate hairpin and Output hairpin. In addition, the freely floating components—Input strand, Fuel complex and Reporter complex—interacted with the localized components to propagate the signal (Fig. 1b). For designing a wire of any length, five unique 6 nt domains (a_o , f , x , y , t) and one 12 nt domain (s) were designed. All the circuit components use a combination of these six domains as specified in Fig. 1b. For the signal crossover, orthogonal 6 nt sequences (x_c , f_c) were allocated to the toehold and hairpin loop domains of participating hairpins as described previously. To design the 2-Input AND domino gate, one more domain (w) was required for the hairpin loop of the Threshold hairpin. The Reporter complex was designed to have an 18 nt double-stranded stem to aid its stability at 25 °C. Accordingly, the Output hairpin was designed to have a 6 nt 3'-flanking domain (t). To design logic circuits with multiple inputs and outputs, Input hairpins with orthogonal 5'-toehold domains (a_o , b_o , c_o , d_o , e_o , f_o) and Output hairpins with orthogonal hairpin loops (y , y_2) were designed. The 3'-flanking domains (grey domains) in the Output hairpins were different for the wires (t) and logic circuits (t_2). All other components in the logic circuits were similar to those used for signal transmission lines. For each localized hairpin at a particular position on the origami, the sequence of the origami staple with its 3' end at that position was extended with the sequence of the corresponding hairpin along its 3' end by a 5 nt polyT linker. The linkers provided conformational flexibility to the hairpins, thus aiding signal propagation on the origami scaffold.

Sequence selection. NUPACK⁴⁴ was used to generate a set of orthogonal 6 nt toeholds and 12 nt stem domains. No more than three Gs, Cs, As or Ts were allowed consecutively, and the ensemble defect was set to 1%. For different circuits, the corresponding number of domains was selected from the master pool to generate individual component sequences. These sequences were then verified by NUPACK to detect possible non-intended interactions and the domains were further optimized if any significant interaction was detected.

Preparation of a localized circuit. We used a twist-corrected version of the rectangular tile origami as a scaffold for our study¹⁰. Twist-correction by base deletion at every third turn on the helical axes has been shown to reduce global twist, thus providing greater predictability in circuit design and improved assembly. We did not add any edge staples to prevent origami edge stacking while annealing¹⁰. For origami preparation, standard desalted DNA staple strands were batch ordered in 96-well plates at stock concentrations of 400 μ M in RNase-free water (Integrated DNA Technologies, IDT) and m13mp18 single-stranded template DNA was purchased from Bayou Biolabs. Modified staple strands with component hairpin sequences at the 3' end, Fuel complex, Input strands and fluorophore-labelled and quencher-labelled strands for different Reporter complexes were ordered with HPLC purification from IDT. In addition, for each Output hairpin, an Output opening strand (OOS) complementary to the 5' toehold and the adjacent stem domain, and for each Reporter complex, a Reporter opening strand (PO) complementary to the fluorophore-labelled strand, were ordered with HPLC purification from IDT, and the lyophilized samples were re-suspended with Tris-EDTA buffer (TE, nuclease free, pH 8.0) to stock concentrations of 100 μ M and stored at -20 °C. Diluted aliquots were further prepared for each of the hairpin staples, as well as the corresponding unmodified staples and other strands as and when needed for regular use, and were stored temporarily at 4 °C. Three master layouts were prepared with the origami scaffold: one for the wires (Supplementary Fig. 1a), one for the logic circuits (excluding dual rail XNOR) (Supplementary Fig. 1b) and one for the dual-rail two-input XNOR circuit (Supplementary Fig. 1c). All circuit operations explained in the study were performed using subsets of these three blueprints. For each blueprint, 4 μ M master stocks (one each for the top and bottom halves of the origami) of staples were prepared, excluding the staples in the blueprint. To prepare a specific wire or logic gate, 1 \times M13mp18 template DNA was mixed with 5 \times the staple master stocks, 10 \times the corresponding modified staples with hairpins and 10 \times the unmodified staples for the rest of the sites for that blueprint. These components were combined in Tris-acetate EDTA buffer with 12.5 mM Mg^{2+} (1 \times Tris-acetate-EDTA (TAE)/ Mg^{2+} : 40 mM Tris base, 20 mM acetic acid, 2 mM EDTA and 12.5 mM magnesium acetate, adjusted to pH 8.0), 1 \times = 60 nM. The reaction mix was then annealed by incubation at 95 °C for 2 min, slow cooling to 60 °C at 0.1 °C every 12 s, incubation at 60 °C for 12 min, slow cooling to 25 °C at 0.1 °C every 12 s, then held at 4 °C for up to 24 h (Annealing Protocol 1).

Stock solutions of 10 μ M Fuel complex were prepared in 1 \times TAE/ Mg^{2+} and annealed by heating to 95 °C for 2 min and slowly cooling to room temperature at 0.1 °C every 6 s (Annealing Protocol 2). The Reporter complexes were annealed following Annealing Protocol 2 after mixing fluorophore-labelled strand and quencher-labelled strand at molar ratios of 1:1.2 in 1 \times TAE/ Mg^{2+} .

Purification of circuit components. Annealed origamis were purified to remove excess staple strands by means of size exclusion chromatography using Sephacryl

S300-HR resin (GE Healthcare Life Sciences). The Sephacryl S300-HR resin was commercially pre-equilibrated in 20% ethanol. Aliquots of Sephacryl S300-HR were collected in 50 ml falcon tubes and centrifuged at 1,000g for 5 min in 4 °C. The supernatants containing ethanol were discarded and the resin pellets were equilibrated three times with distilled water and three times with 1 \times TAE/ Mg^{2+} by re-suspending the pellets with solvents to 50 ml by shaking, centrifugation at 1,000g for 5 min in 4 °C, and discarding the supernatants. After the supernatants were discarded in the final round, the resin pellets were re-suspended with equal volumes of 1 \times TAE/ Mg^{2+} and stored at 4 °C. To prepare each size-exclusion column, 500 μ l of re-suspended resin was added to a 0.8 ml Micro Bio-Spin Chromatography column (Bio-Rad Laboratories) with a collection tube and centrifuged at 1,000g for 5 min at room temperature. The flow-through was discarded and an additional 500 μ l of resin was added to the column before another centrifugation at 1,000g for 5 min at room temperature. Three such columns were prepared for purification of up to 50 μ l of each origami construct. The resultant columns were placed on fresh sterile 1.7 ml Eppendorf tubes and up to 50 μ l of annealed origami was loaded on each column for the first round of purification. Each column was centrifuged at 1,000g for 5 min at room temperature and the flow-through was collected and loaded onto a fresh column for the second round of centrifugation. After repeating the process through a third round, the flow-through for each origami sample was collected for experiments. Supplementary Fig. 2 shows a 1% agarose gel analysis demonstrating the efficiency of the purification protocol. We observe minimal loss of origami with almost complete purification of any excess staples after three rounds of purification.

For the domino wires, the annealed Reporter complex was also run through 10% polyacrylamide gel electrophoresis (PAGE) with 12% glycerol as loading agent, to remove the excess quencher-labelled strand. The band corresponding to the full Reporter complex was visualized using black light and cut out and suspended in 1 \times TAE/ Mg^{2+} for 24 h at room temperature. The resultant solvent was extracted and stored at 4 °C for kinetics experiments.

Fluorescence kinetics experiments. Kinetics experiments were performed on a spectrofluorometer (Horiba Scientific: Fluorolog-3 and FluoroMax-4) with 0.875 ml Fluorometer Micro Square Cells with polytetrafluoroethylene (PTFE) stoppers (Starna: 23-5.45-SOG-5) and cuvette adaptors (Starna: FCA5). A maximum of four samples were tested for each set of measurements using a 5 nm slit width for both excitation and emission monochromators and an integration time of 10 s. Excitation and emission wavelengths of different fluorophores used in various experiments were as follows: FAM (495/520 nm) and Cy5 (648/668 nm). For experiments using a single Reporter, measurements were taken every 60 s, while for experiments using two Reporters, measurements were taken every 120 or 150 s. Before an experiment, the cuvettes were cleaned by washing five times with distilled water, once with 70% ethanol and another five times with distilled water. The excess residual water was dried out of the cuvettes with airflow. Generally, all the circuit components except the Input strand(s) were mixed and added to the cuvettes and an initial steady-state signal for each sample was measured as baseline. The experiment was then paused for the addition of Input strand(s) and subsequent mixing by gentle vortex or inverted shaking. The cuvettes were then put back into the fluorometer, and the experiment was resumed. After completion of data collection for circuit performance, an excess (400 nM) of corresponding OOS was added to trigger the unreacted Output hairpin. The resultant final output signal was representative of the total number of output hairpins and was taken as a close approximation of the total number of origami molecules present in the solution for modelling studies.

Data representation. Arbitrary fluorescence units (S/R values) obtained from the spectrophotometer were first corrected by subtracting the baseline signal values for each sample, as discussed in the previous section. The baseline corrected signal was then converted to concentrations of the corresponding unquenched fluorophore strands using the calibration curve for each Reporter complex (Supplementary Fig. 5). Because we observed small variations in the fluorescence signal at different cuvette positions, calibrations were independently performed for each position. To construct a calibration curve, a predetermined volume of annealed Reporter complex stock was resuspended in 1 \times TAE/ Mg^{2+} , added to the cuvette, and an initial baseline signal was recorded for each cuvette. This was followed by stepwise addition of known concentrations of Reporter-triggering probe opening (PO) strands. After each trigger strand addition, the increase in signal was recorded until a steady-state value was reached. The baseline-corrected signal values were then plotted against the PO strand concentrations to obtain a calibration curve. The signal values were linearly proportional to the fluorophore concentrations, and the slope of a linear fit was recorded as the signal-to-concentration 'conversion factor' for that cuvette position and Reporter. Supplementary Fig. 4 shows an example calibration curve for one of the Reporters used in this study.

Finally, an excess of PO strand was added to the solution to trigger all the Reporter complexes and the final increase in signal was divided by the conversion factor to obtain the actual concentration of the Reporter complex in the solution and in turn the actual concentration of the Reporter complex stock. Importantly, these conversion factors were used to translate the increase in output signal due to signal propagation through a circuit using the corresponding Reporter complex as output. Fresh calibration curves were constructed in the event of a change in external

experimental conditions (for example, different cuvettes, new xenon lamp, different batch of Reporter strands and so on), to maintain accuracy and consistency across different experiments.

Agarose and PAGE. To analyse the purification efficiency using the Sephacryl S300-HR resin purification method, 1% agarose gel was prepared by mixing 1 g of Ultrapure TM agarose (Thermo Fisher Scientific, catalogue no. 16500500) in 100 ml of $1\times$ TAE/ Mg^{2+} . The solution was then heated to boiling point and cooled to 50–60 °C to dissolve the agarose, before pouring it into the gel tray to solidify the gel. The solidified gel was placed in the gel tray in a container with ice such that the side and bottom walls of the gel tray were always in contact with the ice. Pre-cooled $1\times$ TAE/ Mg^{2+} was added as running buffer until the gel was completely submerged in the tray. This prevented over-heating of the gel and the buffer and minimized dissociation of the origamis while running the gel. Origami samples were mixed with appropriate volumes of 80% glycerol to achieve final concentrations of 12% glycerol by volume, which acted as a loading agent. The gel was then run at 100 V for 1 h and stained with SYBR Gold (Thermo Fisher Scientific, catalogue no. S11494) for 15 min before imaging. Gel imaging was performed using a Typhoon FLA 9000 Gel Imaging Scanner (GE Healthcare Life Sciences) at 50 μ m resolution using the SYBR Gold

Nucleic Acid stain filter settings. To purify the Reporter complex used in signal transmission experiments with wires, 10% polyacrylamide gel was prepared by mixing 5 ml 19:1 40% acrylamide/bis, 2 ml $10\times$ Tris-borate-EDTA (TBE)/ Mg^{2+} and deionized water to 20 ml. Then 150 μ l ammonium persulfate (APS) and 15 μ l tetramethylethylenediamine were added to accelerate polymerization of the acrylamide. Annealed Reporter complexes were mixed with 80% glycerol to achieve final concentrations of 12% glycerol by volume and loaded into the wells of the gel (up to 60 μ l of sample per well). PAGE gels were run in $1\times$ TBE/ Mg^{2+} at 120 V for 40 min to separate the excess quencher-labelled strands from the annealed Reporter complexes, then the Reporter complexes were extracted as described before.

Data availability. All relevant data are available from the authors. Requests should be addressed to G.C. and N.D. and/or G.S. and A.P.

References

44. Zadeh, J. *et al.* NUPACK: analysis and design of nucleic acid systems. *J. Comput. Chem.* **32**, 170–173 (2011).